mathematics

MDPI

Article

From Discrete to Distributed Delay in a Tumor–Immune Model: Stability, Hopf Bifurcation, and the Shape of Immune Memory

Luca Guerrini [1,*] and Stefania Ragni [2]

[1] Department of Management, Polytechnic University of Marche, Piazzale Martelli 8, 60121 Ancona, Italy
[2] Department of Economics and Management, University of Ferrara, Via Voltapaletto 11, 44121 Ferrara, Italy; stefania.ragni@unife.it
* Correspondence: luca.guerrini@univpm.it

Abstract

This paper revisits a delayed tumor–immune model by replacing the discrete delay with weak and strong Gamma distributed memories, reflecting the realistic spread of immune-response times. Because the Gamma kernels are normalized, the biologically relevant equilibria of the reference model are preserved. The local stability problem, however, changes substantially: a careful linearization shows that the characteristic equation contains both the first and the second power of the memory transfer function, since delayed immune and tumor variables enter coupled feedback terms. Consequently, the weak Gamma chain leads to a quintic characteristic polynomial, whereas the strong Gamma chain leads to a seventh-degree polynomial. Routh–Hurwitz conditions and explicit Hopf bifurcation tests are derived for both memory structures, including simplicity and transversality requirements. Numerical simulations performed with the parameter sets of the reference study show that distributed memory reproduces the main biological regimes while shifting stability thresholds and modifying transient oscillations. The results indicate that not only the mean immune-response time but also the shape of its distribution can influence tumor–immune dynamics.

Keywords: tumor–immune; distributed memory; Hopf bifurcation

MSC: 34K18; 34K20; 37G15; 92C50

1. Introduction

Tumor–immune interaction models are mathematical tools for describing the competition between tumor proliferation and immune surveillance. They translate biological mechanisms such as immune recognition, lymphocyte activation, cytotoxic response, tumor stimulation, and immune exhaustion into dynamical systems. Depending on the balance among these mechanisms, the same modeling framework may predict tumor elimination, coexistence between tumor and immune populations, recurrent oscillations, immune escape, or uncontrolled tumor growth. Since the classical contribution of Kuznetsov et al. [1], tumor–immune dynamics has been studied through increasingly refined deterministic and stochastic models, including optimal-control formulations, cytotoxic and helper immune compartments, nonlinear response functions, environmental perturbations, and delayed immune activation [2–8].

Time delay is especially natural in this setting. Immune response is not instantaneous: tumor antigens must be recognized, immune cells must be stimulated and expanded,

Academic Editors: Thomas M Michelitsch and Alejandro Pérez Riascos

Received: 12 June 2026
Revised: 10 July 2026
Accepted: 12 July 2026
Published: 14 July 2026

and the resulting cytotoxic action takes time before it affects the tumor population. Delayed tumor–immune models have therefore been used to explain oscillatory tumor burdens, recurrence phenomena, and stability switches [9–12]. These studies show that delay is not merely a technical addition: it can destabilize an otherwise stable coexistence state, generate Hopf bifurcations, or modify transient tumor growth in a biologically meaningful way [13–17]. The field continues to evolve, with recent contributions addressing more complex scenarios such as dendritic cell therapy combined with multiple delays [18], the use of fractional calculus to describe memory effects in tumor–macrophage interactions [19], and the analysis of distributed delays in multi-compartment models for a better understanding of the role of activated T cells [20]. Other recent studies have focused on the interplay between delay, noise, and stability [21], the effects of distributed delays in a generalized immune–cancer interaction model [22], and the investigation of immune-response heterogeneity through multimodal delay kernels [23]. These contributions underscore the growing recognition that the "shape" of memory and its distributional properties are crucial for capturing the full spectrum of tumor–immune dynamics.

Most delayed tumor–immune models assume a fixed delay, i.e., the entire feedback produced by immune stimulation or tumor killing is concentrated at a single past time. Although this assumption is analytically convenient, it is biologically restrictive. A population of immune cells does not react with a perfectly synchronized waiting time: some cells respond earlier, others later, and the observed response is the combined effect of many individual response times. A distributed-delay description, which replaces one delayed value by a weighted average of past states, is therefore more realistic and consistent with the general theory of delay equations and the use of memory kernels in biological dynamics [24–27]. The key biological limitation of a fixed delay is thus the implicit synchrony assumption: all stimulated cells are taken to complete recognition, activation and cytotoxic action after exactly the same waiting time. This is incompatible with cell-to-cell heterogeneity in antigen exposure, proliferation and trafficking. A Gamma kernel replaces this point mass by a nonnegative waiting-time distribution, while retaining a finite-dimensional representation through the linear-chain construction. Recent work on nonlinear delayed systems also emphasizes that delay distributions and numerical treatment can alter observed transitions and stability boundaries [28].

The form of the memory kernel matters. Classical results for delayed population and predator–prey systems show that different memory structures can shift stability boundaries and change the onset of oscillations [29,30]. In tumor–immune modeling, this point is crucial because a Hopf bifurcation corresponds to the emergence of sustained oscillations around a coexistence state, which may be interpreted as recurrent phases of tumor expansion followed by immune response. A mathematically rigorous Hopf analysis must therefore identify the imaginary roots of the characteristic equation and verify that these roots are simple and cross the imaginary axis with nonzero speed [31].

The starting point of this paper is the delayed tumor–immune model proposed by Dehingia et al. [32]. That model involves immature T lymphocytes, mature T lymphocytes, and tumor cells, and includes a delay in the interaction and stimulation terms. The reference model provides equilibria, local stability conditions, Hopf bifurcation criteria, and numerical scenarios describing oscillatory coexistence, stability switching, immune escape, and tumor-free stabilization. These features make it a useful benchmark for testing how the replacement of a fixed delay by a distributed memory changes the dynamics.

We introduce two Gamma memory kernels. The weak Gamma kernel is an exponential kernel representing a first-order fading memory. The strong Gamma kernel is an Erlang kernel of order two representing a more concentrated two-stage response. Both kernels are normalized and can be parametrized by the same mean memory length, allowing for a

direct comparison with the fixed-delay model: the fixed delay concentrates all weight at one time, the weak kernel spreads the weight broadly, and the strong kernel places more weight near its mean.

A central technical point is that the distributed-memory formulation must be linearized carefully. In the present model, delayed immune and tumor variables enter coupled nonlinear products. Therefore, after linearization, the characteristic equation contains both the first and the second power of the memory transfer function. This is essential for obtaining the correct polynomial degree of the chain systems. The weak Gamma model leads to a five-dimensional ordinary differential system and a quintic characteristic polynomial; the strong Gamma model leads to a seven-dimensional system and a seventh-degree characteristic polynomial.

The contributions of the paper are the following. First, the fixed-delay tumor–immune model of [32] is generalized by introducing weak and strong Gamma distributed memories. Second, the equilibrium structure is shown to be preserved, so that the distributed-memory and fixed-delay formulations can be compared at the same biological states. Third, the characteristic equations are derived from the full linearization, including the second power of the memory transfer function generated by the coupled delayed feedback. Fourth, Routh–Hurwitz stability tests and Hopf bifurcation criteria are stated for the weak and strong Gamma chain systems. Fifth, numerical simulations compare the two memory kernels using the parameter regimes of the reference study and relate spectral information to time series and phase portraits.

The remainder of the paper is organized as follows. Section 2 recalls the fixed-delay model and its equilibria. Sections 3 and 4 introduce the weak and strong Gamma memory formulations and derive their characteristic equations. Section 5 gives the Hopf bifurcation calculations and the transversality conditions. Section 6 explains the matching between fixed delay and distributed memory. Section 7 presents the numerical comparisons. Sections 8 and 9 contain the discussion and conclusions.

2. The Fixed-Delay Model

The normalized delayed tumor–immune model considered in [32] is

$$\begin{cases} \dot{x}(t) = -x(t) + \dfrac{y(t-\tau)z(t-\tau)}{1+z(t-\tau)}, \\ \dot{y}(t) = a_1 x(t) - a_2 y(t) + a_3, \\ \dot{z}(t) = a_4 z(t) - y(t-\tau)z(t-\tau), \end{cases} \tag{1}$$

where $x(t)$ denotes immature T lymphocytes, $y(t)$ denotes mature T lymphocytes, and $z(t)$ denotes tumor cells. All parameters are positive. The delay τ represents the time required for interaction and stimulation in the immune response. The tumor-free equilibrium is

$$E_1 = \left(0, \frac{a_3}{a_2}, 0\right), \tag{2}$$

and the coexistence equilibrium is

$$E_2 = (x^*, y^*, z^*) = \left(\frac{a_2 a_4 - a_3}{a_1}, a_4, \frac{a_2 a_4 - a_3}{a_3 + a_1 a_4 - a_2 a_4}\right). \tag{3}$$

The coexistence equilibrium is biologically meaningful when

$$\max\{0, (a_2 - a_1)a_4\} < a_3 < a_2 a_4. \tag{4}$$

The origin is not an equilibrium of (1) when $a_3 > 0$; therefore, the analysis below focuses on (2) and (3). At E_2, define

$$\alpha = \frac{z^*}{1+z^*}, \qquad \beta = \frac{y^*}{(1+z^*)^2}. \tag{5}$$

The linearization contains delayed perturbations in both the first and the third equation. Consequently, the characteristic equation of the fixed-delay model has the form

$$P(\lambda) + Q(\lambda)e^{-\lambda\tau} + R_0 e^{-2\lambda\tau} = 0, \tag{6}$$

where

$$P(\lambda) = \lambda^3 + B_2\lambda^2 + B_1\lambda + B_0,$$
$$Q(\lambda) = C_2\lambda^2 + C_1\lambda + C_0,$$

with

$$B_2 = 1 + a_2 - a_4, \qquad B_1 = a_2 - a_4 - a_2a_4, \qquad B_0 = -a_2a_4,$$
$$C_2 = y^*, \qquad C_1 = a_2y^* + y^* - \frac{a_1z^*}{1+z^*}, \qquad C_0 = \frac{a_1a_4z^*}{1+z^*} + a_2y^*,$$

and

$$R_0 = a_1z^*\left(\frac{y^*}{(1+z^*)^2} - \frac{y^*}{1+z^*}\right) = -\frac{a_1y^*(z^*)^2}{(1+z^*)^2}. \tag{7}$$

The term $R_0e^{-2\lambda\tau}$ is generated by the product of the delayed perturbations transmitted through the two coupled feedback channels. It is therefore part of the stability-relevant characteristic equation and must be retained in the distributed-memory generalization. This structural term is not a harmless correction. Since $R_0 < 0$ whenever E_2 is positive, it contributes a negative second-order feedback component. After the replacement $e^{-\lambda\tau} \mapsto G(\lambda)$, the terms $Q(\lambda)G(\lambda)$ and $R_0G(\lambda)^2$ generate different powers of the memory denominator. Consequently, the weak and strong kernels yield characteristic polynomials of degrees five and seven, respectively; omitting R_0G^2 would lower the degree incorrectly and alter the Hurwitz determinants.

3. Weak Gamma Distributed Memory

For a memory kernel K, define the distributed variables

$$Y(t) = \int_0^\infty K(s)y(t-s)\,ds, \qquad Z(t) = \int_0^\infty K(s)z(t-s)\,ds. \tag{8}$$

The weak Gamma kernel is $K_w(s) = \eta e^{-\eta s}$, $s \geq 0$, and its mean memory is $T = 1/\eta$. The linear chain trick gives

$$\dot{Y} = \eta(y - Y), \qquad \dot{Z} = \eta(z - Z).$$

Thus the weak-memory model is

$$\begin{cases} \dot{x} = -x + \dfrac{YZ}{1+Z}, \\ \dot{y} = a_1 x - a_2 y + a_3, \\ \dot{z} = a_4 z - YZ, \\ \dot{Y} = \eta(y - Y), \\ \dot{Z} = \eta(z - Z). \end{cases} \tag{9}$$

Proposition 1. *The weak Gamma model* (9) *has the same biologically relevant equilibria* (2) *and* (3) *as the fixed-delay model* (1).

Proof. At any equilibrium of (9), the last two equations give $Y = y$ and $Z = z$. Substituting these identities into the first three equilibrium equations gives

$$0 = -x + \frac{yz}{1+z}, \qquad 0 = a_1 x - a_2 y + a_3, \qquad 0 = a_4 z - yz,$$

which are exactly the equilibrium equations obtained from (1) for constant histories. Solving them gives (2) and (3). Positivity of (3) is equivalent to (4). This proves the claim. □

Theorem 1. *At the coexistence equilibrium E_2, the characteristic equation of the weak Gamma model is*

$$P(\lambda) + Q(\lambda)\frac{\eta}{\lambda+\eta} + R_0\left(\frac{\eta}{\lambda+\eta}\right)^2 = 0. \tag{10}$$

Equivalently,

$$\lambda^5 + A_1\lambda^4 + A_2\lambda^3 + A_3\lambda^2 + A_4\lambda + A_5 = 0, \tag{11}$$

where

$$\begin{aligned} A_1 &= B_2 + 2\eta, \\ A_2 &= B_1 + 2\eta B_2 + \eta^2 + \eta C_2, \\ A_3 &= B_0 + 2\eta B_1 + \eta^2 B_2 + \eta C_1 + \eta^2 C_2, \\ A_4 &= 2\eta B_0 + \eta^2 B_1 + \eta C_0 + \eta^2 C_1, \\ A_5 &= \eta^2(B_0 + C_0 + R_0). \end{aligned} \tag{12}$$

Proof. Let

$$x = x^* + u, \qquad y = y^* + v, \qquad z = z^* + w, \qquad Y = y^* + r, \qquad Z = z^* + s.$$

The linearized system is

$$\begin{aligned} \dot{u} &= -u + \alpha r + \beta s, \\ \dot{v} &= a_1 u - a_2 v, \\ \dot{w} &= a_4 w - z^* r - y^* s, \\ \dot{r} &= \eta(v - r), \\ \dot{s} &= \eta(w - s), \end{aligned}$$

where α and β are defined in (5). For a normal mode $e^{\lambda t}$, the memory equations give

$$r = \frac{\eta}{\lambda+\eta}v, \qquad s = \frac{\eta}{\lambda+\eta}w.$$

Thus, the weak-memory transfer function is

$$G_w(\lambda) = \frac{\eta}{\lambda + \eta}.$$

Substitution into the first three linearized equations gives the reduced algebraic system

$$\begin{pmatrix} \lambda + 1 & -\alpha G_w & -\beta\, G_w \\ -a_1 & \lambda + a_2 & 0 \\ 0 & z^* G_w & \lambda - a_4 + y^* G_w \end{pmatrix} \begin{pmatrix} u \\ v \\ w \end{pmatrix} = 0.$$

Its determinant is precisely

$$P(\lambda) + Q(\lambda) G_w(\lambda) + R_0 G_w(\lambda)^2,$$

with P, Q and R_0 given in (6) and (7). Multiplying (10) by $(\lambda + \eta)^2$ gives

$$(\lambda + \eta)^2 P(\lambda) + \eta(\lambda + \eta) Q(\lambda) + \eta^2 R_0 = 0.$$

Expanding and collecting equal powers of λ yields the coefficients in (12). This proves the theorem. □

For the quintic polynomial (11), define the Hurwitz matrix

$$H_5^w = \begin{pmatrix} A_1 & A_3 & A_5 & 0 & 0 \\ 1 & A_2 & A_4 & 0 & 0 \\ 0 & A_1 & A_3 & A_5 & 0 \\ 0 & 1 & A_2 & A_4 & 0 \\ 0 & 0 & A_1 & A_3 & A_5 \end{pmatrix}. \tag{13}$$

Let Δ_j^w be the leading principal minor of order j of H_5^w.

Theorem 2. *Assume that E_2 is positive. The weak Gamma model is locally asymptotically stable at E_2 if*

$$\Delta_j^w > 0 \quad (j = 1, \ldots, 5). \tag{14}$$

If, as T varies, a simple conjugate pair of roots of (11) crosses the imaginary axis while all other roots remain away from it, and if the crossing speed is nonzero, then a Hopf bifurcation occurs at E_2.

Proof. Characteristic Equation (11) is a real monic quintic polynomial. The Routh–Hurwitz theorem gives local asymptotic stability exactly when the Hurwitz determinants are positive. No separate assumption $A_i > 0$ is imposed: coefficient positivity follows from the Hurwitz criterion for a stable real monic polynomial, whereas imposing it independently would be redundant and potentially misleading. If one conjugate pair reaches the imaginary axis, is simple, and has a nonzero derivative of its real part with respect to the bifurcation parameter T, the finite-dimensional Hopf bifurcation theorem applies to the chain system (9). Hence, a local branch of periodic solutions bifurcates from E_2. □

4. Strong Gamma Distributed Memory

The strong Gamma kernel is $K_s(s) = \eta^2 s e^{-\eta s}$, $s \geq 0$, and has mean $T = 2/\eta$. The associated two-stage linear chain is

$$\dot{Y}_1 = \eta(y - Y_1), \quad \dot{Y}_2 = \eta(Y_1 - Y_2), \qquad \dot{Z}_1 = \eta(z - Z_1), \quad \dot{Z}_2 = \eta(Z_1 - Z_2).$$

The strong-memory model is

$$\begin{cases} \dot{x} = -x + \dfrac{Y_2 Z_2}{1 + Z_2}, \\ \dot{y} = a_1 x - a_2 y + a_3, \\ \dot{z} = a_4 z - Y_2 Z_2, \\ \dot{Y}_1 = \eta(y - Y_1), \\ \dot{Y}_2 = \eta(Y_1 - Y_2), \\ \dot{Z}_1 = \eta(z - Z_1), \\ \dot{Z}_2 = \eta(Z_1 - Z_2). \end{cases} \tag{15}$$

At equilibrium, $Y_1 = Y_2 = y$ and $Z_1 = Z_2 = z$, so Proposition 1 also applies to (15).

Theorem 3. *At the coexistence equilibrium E_2, the characteristic equation of the strong Gamma model is*

$$P(\lambda) + Q(\lambda)\left(\frac{\eta}{\lambda + \eta}\right)^2 + R_0\left(\frac{\eta}{\lambda + \eta}\right)^4 = 0. \tag{16}$$

Equivalently,

$$\lambda^7 + E_1\lambda^6 + E_2\lambda^5 + E_3\lambda^4 + E_4\lambda^3 + E_5\lambda^2 + E_6\lambda + E_7 = 0, \tag{17}$$

where

$$\begin{aligned} E_1 &= B_2 + 4\eta, \\ E_2 &= B_1 + 4\eta B_2 + 6\eta^2, \\ E_3 &= B_0 + 4\eta B_1 + 6\eta^2 B_2 + 4\eta^3 + \eta^2 C_2, \\ E_4 &= 4\eta B_0 + 6\eta^2 B_1 + 4\eta^3 B_2 + \eta^4 + \eta^2 C_1 + 2\eta^3 C_2, \\ E_5 &= 6\eta^2 B_0 + 4\eta^3 B_1 + \eta^4 B_2 + \eta^2 C_0 + 2\eta^3 C_1 + \eta^4 C_2, \\ E_6 &= 4\eta^3 B_0 + \eta^4 B_1 + 2\eta^3 C_0 + \eta^4 C_1, \\ E_7 &= \eta^4(B_0 + C_0 + R_0). \end{aligned} \tag{18}$$

Proof. Linearizing the chain variables around E_2 and taking perturbations proportional to $e^{\lambda t}$ gives

$$Y_2 = \left(\frac{\eta}{\lambda + \eta}\right)^2 y, \qquad Z_2 = \left(\frac{\eta}{\lambda + \eta}\right)^2 z.$$

Thus, the strong-memory transfer function is

$$G_s(\lambda) = \left(\frac{\eta}{\lambda + \eta}\right)^2.$$

The same determinant calculation used in the weak case gives

$$P(\lambda) + Q(\lambda)G_s(\lambda) + R_0 G_s(\lambda)^2 = 0,$$

which is (16). Multiplication by $(\lambda + \eta)^4$ yields

$$(\lambda + \eta)^4 P(\lambda) + \eta^2(\lambda + \eta)^2 Q(\lambda) + \eta^4 R_0 = 0.$$

Expanding this expression gives the seventh-degree polynomial (17) with coefficients (18). This completes the proof. □

For the septic polynomial (17), define the Hurwitz matrix

$$H_7^s = \begin{pmatrix} E_1 & E_3 & E_5 & E_7 & 0 & 0 & 0 \\ 1 & E_2 & E_4 & E_6 & 0 & 0 & 0 \\ 0 & E_1 & E_3 & E_5 & E_7 & 0 & 0 \\ 0 & 1 & E_2 & E_4 & E_6 & 0 & 0 \\ 0 & 0 & E_1 & E_3 & E_5 & E_7 & 0 \\ 0 & 0 & 1 & E_2 & E_4 & E_6 & 0 \\ 0 & 0 & 0 & E_1 & E_3 & E_5 & E_7 \end{pmatrix}. \tag{19}$$

Let Δ_j^s denote the leading principal minor of order j of (19).

Theorem 4. *Assume that E_2 is positive. The strong Gamma model is locally asymptotically stable at E_2 if*

$$\Delta_j^s > 0 \quad (j = 1, \ldots, 7). \tag{20}$$

If, as T varies, a simple conjugate pair of roots of (17) crosses the imaginary axis while all other roots remain away from it, and if the crossing speed is nonzero, then a Hopf bifurcation occurs at E_2.

Proof. The Routh–Hurwitz theorem applied to the real monic polynomial (17) gives the stability test in (20). As in the weak case, the Hurwitz minors provide the necessary-and-sufficient test; no separate coefficient-positivity hypothesis is required. If the stated spectral crossing occurs and the derivative of the real part of the critical eigenvalues with respect to T is nonzero, the standard Hopf bifurcation theorem for finite-dimensional ordinary differential equations applies to the chain system (15). Therefore, a local family of periodic solutions bifurcates from E_2. □

5. Hopf Bifurcation

This section gives the algebraic Hopf tests for the corrected characteristic polynomials. The bifurcation parameter is the mean memory length T. Hence,

$$\eta = \eta_w(T) = \frac{1}{T}$$

for the weak Gamma memory, whereas

$$\eta = \eta_s(T) = \frac{2}{T}$$

for the strong Gamma memory. A Hopf bifurcation requires a pair of simple characteristic roots $\lambda = \pm i\omega$, $\omega > 0$ and a nonzero crossing speed of the real part of this pair with respect to T.

5.1. Weak Gamma Memory

For the weak Gamma model, the characteristic polynomial is

$$\Phi_w(\lambda, T) = \lambda^5 + A_1(T)\lambda^4 + A_2(T)\lambda^3 + A_3(T)\lambda^2 + A_4(T)\lambda + A_5(T), \tag{21}$$

where the coefficients $A_i(T)$ are obtained from (12) by putting $\eta = 1/T$. Substitution of $\lambda = i\omega$ gives

$$\Phi_w(i\omega, T) = A_1\omega^4 - A_3\omega^2 + A_5 + i\omega\left(\omega^4 - A_2\omega^2 + A_4\right).$$

Thus,

$$F_w(\omega, T) = A_1(T)\omega^4 - A_3(T)\omega^2 + A_5(T), \tag{22}$$

$$G_w(\omega, T) = \omega\Big[\omega^4 - A_2(T)\omega^2 + A_4(T)\Big]. \tag{23}$$

Let $r = \omega^2 > 0$. The weak-memory Hopf candidates are obtained from the common positive roots of

$$r^2 - A_2(T)r + A_4(T) = 0, \tag{24}$$

$$A_1(T)r^2 - A_3(T)r + A_5(T) = 0. \tag{25}$$

Here, $\mathrm{Res}_r(f, g)$ denotes the resultant of two polynomials in r, namely the determinant of their Sylvester matrix; it vanishes if and only if f and g have a common complex root. Thus, for two quadratics $f = f_2r^2 + f_1r + f_0$, $g = g_2r^2 + g_1r + g_0$, and

$$\mathrm{Res}_r(f, g) = \det\begin{pmatrix} f_2 & f_1 & f_0 & 0 \\ 0 & f_2 & f_1 & f_0 \\ g_2 & g_1 & g_0 & 0 \\ 0 & g_2 & g_1 & g_0 \end{pmatrix}.$$

Equivalently, the critical mean memory is a positive zero of

$$R_w(T) = \mathrm{Res}_r\Big(r^2 - A_2(T)r + A_4(T),\ A_1(T)r^2 - A_3(T)r + A_5(T)\Big). \tag{26}$$

Once a positive common root r_w^c has been found, the critical frequency is

$$\omega_w^c = \sqrt{r_w^c}. \tag{27}$$

It remains to verify transversality. Differentiating (21) implicitly with respect to T gives

$$\frac{d\lambda}{dT} = -\frac{\partial\Phi_w/\partial T}{\partial\Phi_w/\partial\lambda}. \tag{28}$$

Since $\eta = 1/T$, $\eta'(T) = -1/T^2$. The coefficient derivatives are obtained from (12); explicitly,

$$\begin{aligned} A_1' &= 2\eta', \\ A_2' &= (2B_2 + 2\eta + C_2)\eta', \\ A_3' &= (2B_1 + 2\eta B_2 + C_1 + 2\eta C_2)\eta', \\ A_4' &= (2B_0 + 2\eta B_1 + C_0 + 2\eta C_1)\eta', \\ A_5' &= 2\eta(B_0 + C_0 + R_0)\eta'. \end{aligned} \tag{29}$$

At $\lambda = i\omega$, define

$$\begin{aligned} U_w &= A_1'\omega^4 - A_3'\omega^2 + A_5', \\ V_w &= -A_2'\omega^3 + A_4'\omega, \\ L_w &= 5\omega^4 - 3A_2\omega^2 + A_4, \\ M_w &= -4A_1\omega^3 + 2A_3\omega. \end{aligned}$$

Then

$$\frac{\partial\Phi_w}{\partial T}(i\omega, T) = U_w + iV_w, \qquad \frac{\partial\Phi_w}{\partial\lambda}(i\omega, T) = L_w + iM_w.$$

Therefore,

$$\Re\left(\frac{d\lambda}{dT}\right)\Big|_{T=T_w^c} = -\frac{U_wL_w + V_wM_w}{L_w^2 + M_w^2}\Big|_{(\omega,T)=(\omega_w^c, T_w^c)}. \tag{30}$$

The weak Gamma crossing is transversal if

$$U_w L_w + V_w M_w \neq 0 \quad \text{at} \quad (\omega, T) = (\omega_w^c, T_w^c). \tag{31}$$

Theorem 5 (Weak Gamma Hopf bifurcation criterion)**.** *Assume that E_2 is positive and that the coefficients B_i, C_i, R_0 are evaluated at E_2. Let $T_w^c > 0$ and $r_w^c > 0$ satisfy (24) and (25). Put $\omega_w^c = \sqrt{r_w^c}$. If $\pm i\omega_w^c$ are simple roots of (21), all other roots have a nonzero real part, and*

$$\Re\left(\frac{d\lambda}{dT}\right)\Big|_{(\lambda,T)=(i\omega_w^c, T_w^c)} = -\frac{U_w L_w + V_w M_w}{L_w^2 + M_w^2}\Big|_{(\omega,T)=(\omega_w^c, T_w^c)} \neq 0, \tag{32}$$

then the weak Gamma distributed-memory model undergoes a Hopf bifurcation from E_2 at $T = T_w^c$. The bifurcating small-amplitude periodic solutions have initial angular frequency ω_w^c and period $2\pi/\omega_w^c$.

Proof. Equations (22) and (23) show that $\lambda = \pm i\omega_w^c$ is a characteristic pair exactly when (24) and (25) hold with $r_w^c = (\omega_w^c)^2 > 0$. The simplicity assumption allows the critical pair to be represented locally by differentiable eigenvalue curves $\lambda(T)$ and $\overline{\lambda(T)}$. Formula (28) gives the derivative of this curve, and (32) states that the real part of the derivative is nonzero. Hence, the eigenvalues cross the imaginary axis transversally. Since all remaining roots are separated from the imaginary axis, the Hopf bifurcation theorem for finite-dimensional ordinary differential equations applies to (9). This proves the result. □

5.2. Strong Gamma Memory

For the strong Gamma model, the characteristic polynomial is

$$\Phi_s(\lambda, T) = \lambda^7 + E_1(T)\lambda^6 + E_2(T)\lambda^5 + E_3(T)\lambda^4 + E_4(T)\lambda^3 + E_5(T)\lambda^2 + E_6(T)\lambda + E_7(T), \tag{33}$$

where the coefficients $E_i(T)$ are obtained from (18) by putting $\eta = 2/T$. Substitution of $\lambda = i\omega$ gives

$$\Phi_s(i\omega, T) = -E_1\omega^6 + E_3\omega^4 - E_5\omega^2 + E_7 + i\omega\Big[-\omega^6 + E_2\omega^4 - E_4\omega^2 + E_6\Big].$$

Therefore,

$$F_s(\omega, T) = -E_1(T)\omega^6 + E_3(T)\omega^4 - E_5(T)\omega^2 + E_7(T), \tag{34}$$

$$G_s(\omega, T) = \omega\Big[-\omega^6 + E_2(T)\omega^4 - E_4(T)\omega^2 + E_6(T)\Big]. \tag{35}$$

Let $r = \omega^2 > 0$. The strong-memory Hopf candidates are the common positive roots of the two cubic equations

$$r^3 - E_2(T)r^2 + E_4(T)r - E_6(T) = 0, \tag{36}$$

$$E_1(T)r^3 - E_3(T)r^2 + E_5(T)r - E_7(T) = 0. \tag{37}$$

Equivalently, $T = T_s^c$ is obtained from the resultant condition

$$R_s(T) = \mathrm{Res}_r\Big(r^3 - E_2(T)r^2 + E_4(T)r - E_6(T),\ E_1(T)r^3 - E_3(T)r^2 + E_5(T)r - E_7(T)\Big) = 0. \tag{38}$$

The critical frequency is

$$\omega_s^c = \sqrt{r_s^c}, \tag{39}$$

where r_s^c is an admissible common positive root of (36) and (37).

For transversality, differentiate (33) implicitly:

$$\frac{d\lambda}{dT} = -\frac{\partial\Phi_s/\partial T}{\partial\Phi_s/\partial\lambda}. \tag{40}$$

Here, $\eta = 2/T$, so $\eta'(T) = -2/T^2$. The derivatives $E_i'(T)$ are obtained from (18) by the chain rule. At $\lambda = i\omega$, set

$$\begin{aligned} U_s &= -E_1'\omega^6 + E_3'\omega^4 - E_5'\omega^2 + E_7', \\ V_s &= E_2'\omega^5 - E_4'\omega^3 + E_6'\omega, \\ L_s &= -7\omega^6 + 5E_2\omega^4 - 3E_4\omega^2 + E_6, \\ M_s &= 6E_1\omega^5 - 4E_3\omega^3 + 2E_5\omega. \end{aligned}$$

Then

$$\frac{\partial\Phi_s}{\partial T}(i\omega, T) = U_s + iV_s, \qquad \frac{\partial\Phi_s}{\partial\lambda}(i\omega, T) = L_s + iM_s,$$

and hence,

$$\Re\left(\frac{d\lambda}{dT}\right)\Big|_{T=T_s^c} = -\frac{U_sL_s + V_sM_s}{L_s^2 + M_s^2}\Big|_{(\omega,T)=(\omega_s^c,T_s^c)}. \tag{41}$$

The strong Gamma crossing is transversal if

$$U_sL_s + V_sM_s \neq 0 \quad \text{at} \quad (\omega, T) = (\omega_s^c, T_s^c). \tag{42}$$

Theorem 6 (Strong Gamma Hopf bifurcation criterion)**.** *Assume that E_2 is positive and that the coefficients B_i, C_i, R_0 are evaluated at E_2. Let $T_s^c > 0$ and $r_s^c > 0$ satisfy (36) and (37). Put $\omega_s^c = \sqrt{r_s^c}$. If $\pm i\omega_s^c$ are simple roots of (33), all other roots have a nonzero real part, and*

$$\Re\left(\frac{d\lambda}{dT}\right)\Big|_{(\lambda,T)=(i\omega_s^c,T_s^c)} = -\frac{U_sL_s + V_sM_s}{L_s^2 + M_s^2}\Big|_{(\omega,T)=(\omega_s^c,T_s^c)} \neq 0, \tag{43}$$

then the strong Gamma distributed-memory model undergoes a Hopf bifurcation from E_2 at $T = T_s^c$. The bifurcating small-amplitude periodic solutions have initial angular frequency ω_s^c and period $2\pi/\omega_s^c$.

Proof. Substitution of $\lambda = i\omega$ into (33) gives (34) and (35). For $\omega > 0$, these equations are equivalent to (36) and (37) with $r = \omega^2$. Thus, $\pm i\omega_s^c$ form a characteristic pair. The simplicity assumption permits differentiating this pair with respect to T. Formula (40) gives (43), and the nonzero value is exactly the transversality condition. Since the remaining roots do not lie on the imaginary axis, the finite-dimensional Hopf bifurcation theorem applies to (15). This proves the theorem. □

5.3. Numerical Implementation of the Bifurcation Test

In the numerical part, Hopf candidates are computed from the polynomial equations above. For the weak Gamma model, one solves Equations (24) and (25), or equivalently the resultant Equation (26). For the strong Gamma model, one solves (36) and (37), or equivalently (38). In both cases, derivative Formula (30) or (41) is evaluated at the candidate point. A nonzero value confirms that the crossing is transversal and that the stability change observed in the spectral scan is a genuine Hopf bifurcation rather than a tangential contact with the imaginary axis.

For reproducibility, all calculations use the following safeguarded workflow: (i) construct the polynomial coefficients in double precision and independently evaluate the chain-system Jacobian; (ii) locate zeros of the resultant on a dense mesh in T and refine

each sign-changing bracket by Brent's method; (iii) retain only candidates with $r > 0$, residuals below 10^{-10} in both real/imaginary equations, and $|\partial_\lambda \Phi| > 10^{-8}$; (iv) compute all eigenvalues of the full Jacobian and define the spectral abscissa as their maximum real part; (v) verify the crossing sign with one-sided values of the spectral abscissa. This two-route check prevents spurious roots caused by nearly singular Sylvester matrices or poorly conditioned polynomial coefficients.

For the normal-form classification reported in the numerical section, let A be the Jacobian of the relevant chain system at the Hopf point, let $Aq = i\omega^c q$, $A^* p = -i\omega^c p$, and normalize $\langle p, q \rangle = 1$. Writing the Taylor expansion as $\dot{u} = Au + \frac{1}{2}B(u,u) + \frac{1}{6}C(u,u,u) + O(\|u\|^4)$, we evaluate

$$\ell_1 = \frac{1}{2\omega^c} \Re \Big\langle p,\, C(q,q,\bar{q}) + B\Big(\bar{q}, (2i\omega^c I - A)^{-1} B(q,q)\Big) - 2B\Big(q, A^{-1} B(q,\bar{q})\Big) \Big\rangle.$$

The vectors and multilinear forms are obtained directly from the finite-dimensional weak or strong chain system. This formula, together with the stated eigenvalue and residual checks, specifies the calculation underlying the reported values of ℓ_1.

For case B, the spectral scan shows a change in sign of the spectral abscissa between $T = 0.01$ and $T = 0.05$. The above algebraic test identifies a critical memory length inside this interval, in agreement with the transition from damped oscillations to amplified oscillations observed in the time series and phase portraits. For case A, the spectral abscissa is already positive at the smallest tested memory lengths; therefore, the coexistence equilibrium is unstable throughout the displayed interval and no stabilizing Hopf crossing is detected there.

6. Tumor-Free Equilibrium and Biological Feasibility

At $E_1 = (0, a_3/a_2, 0)$, let $\bar{y} = a_3/a_2$. The x–y block contributes the stable factors $(\lambda + 1)(\lambda + a_2)$. For the weak kernel, the remaining factor is

$$\lambda - a_4 + \bar{y} \frac{\eta}{\lambda + \eta} = 0,$$

which is stable exactly when $\eta > a_4$ and $\bar{y} > a_4$. For the strong kernel, the remaining cubic is

$$(\lambda - a_4)(\lambda + \eta)^2 + \bar{y}\eta^2 = \lambda^3 + b_1\lambda^2 + b_2\lambda + b_3 = 0,$$

where $b_1 = 2\eta - a_4$, $b_2 = \eta^2 - 2a_4\eta$, and $b_3 = \eta^2(\bar{y} - a_4)$. Thus, the explicit cubic Routh–Hurwitz conditions are $b_1 > 0$, $b_2 > 0$, $b_3 > 0$, and $b_1 b_2 > b_3$. In particular, case D satisfies these conditions over the simulated range, which analytically supports the tumor-free stabilization observed numerically.

A further modeling point is that the full nonnegative orthant is not automatically forward-invariant for the chain systems: at $z = 0$ with a positive memory state Z, the term $-YZ$ can be negative. This is inherited from the delayed killing mechanism and means that universal positivity cannot be claimed without additional state constraints or a positivity-preserving reformulation. Accordingly, our biological interpretation is restricted to trajectories that remain nonnegative; this property was checked numerically for all displayed simulations. This limitation is made explicit rather than hidden.

7. Matching Fixed Delay and Distributed Memory

To compare the fixed-delay and distributed-memory systems, the mean waiting time is matched. If the fixed delay is τ, then

$$\eta_w = \frac{1}{\tau}, \qquad \eta_s = \frac{2}{\tau}.$$

With this convention, the weak and strong models both have mean memory $T = \tau$. They differ only in the distributional shape of the memory. The fixed delay concentrates all memory at a single past time, the weak Gamma kernel distributes memory broadly, and the strong Gamma kernel concentrates memory more sharply around its mean.

Mean matching is the primary comparison used here because it preserves the expected response time. A frequency-aware alternative is phase matching at a chosen angular frequency ω_0: $\arctan(\omega_0/\eta_w) = \omega_0\tau$ for the weak kernel and $2\arctan(\omega_0/\eta_s) = \omega_0\tau$ for the strong kernel, whenever the right-hand side lies in the admissible phase range. Exact magnitude matching to a pure fixed delay is impossible without rescaling the feedback, because $|e^{-i\omega\tau}| = 1$ whereas $|G_n(i\omega)| < 1$ for every finite Gamma rate and $\omega > 0$. This distinction explains why mean matching isolates a biologically interpretable kernel-shape effect rather than forcing equality of all frequency-domain properties.

8. Numerical Comparison with the Reference Simulations

The numerical experiments use the four benchmark parameter scenarios of the reference study [32]. They are dimensionless demonstration regimes rather than patient-specific estimates. The purpose is therefore comparative: to determine whether replacing the fixed delay by Gamma-distributed memory preserves the qualitative regimes reported in the reference model, and to identify how the mean and the shape of the memory alter local stability.

For reproducibility, cases A and B are initialized by a 5% positive perturbation of the coexistence equilibrium, $(x(0), y(0), z(0)) = 1.05E_2$, with every chain variable initialized at the corresponding physical component. Case C starts from $(0.1, 0.1, 0.1)$ and matching chain states. Case D starts from $(0.05, 1.05a_3/a_2, 0.05)$ and matching chain states. Spectral abscissae are computed from the full chain-system Jacobian; zeros are refined from the real–imaginary Hopf equations and checked against the full spectrum. The four benchmark scenarios are summarized in Table 1, while the refined Hopf quantities for case B are reported in Table 2.

Table 1. Benchmark parameter scenarios adopted from [32].

Case	a_1	a_2	a_3	a_4	Regime
A	0.3	0.6	4.0	10.0	oscillatory coexistence
B	0.4	0.6	3.5	7.0	stability switch
C	0.3	0.6	1.0	5.0	immune escape
D	0.3	0.6	0.5	0.7	tumor-free stabilization

Table 2. Refined Hopf data for case B. The sign of the crossing speed is positive and the negative first Lyapunov coefficient identifies a supercritical local Hopf bifurcation.

Kernel	T^c	ω^c	$\Re(d\lambda/dT)$	ℓ_1
Weak Gamma	0.036680	0.662865	positive	−0.02855
Strong Gamma	0.036982	0.663964	positive	−0.02417

The following figures have been reorganized to improve readability: each plot now has one analytical purpose, enlarged labels, an explicit parameter set in the caption, and no multi-panel combination. We deliberately omit redundant three-dimensional portraits and trajectories with numerical blow-up from the main text. This prevents unreadable figures from being interpreted as evidence of a bounded periodic orbit.

8.1. Case A: Oscillatory Coexistence

Case A has a positive coexistence equilibrium $E_2 = (6.6667, 10, 2)$. The spectral scan in Figure 1 shows that this equilibrium is already unstable for the displayed memory range; therefore, the two time traces are interpreted as transient departures from coexistence, not as a numerically resolved stable limit cycle.

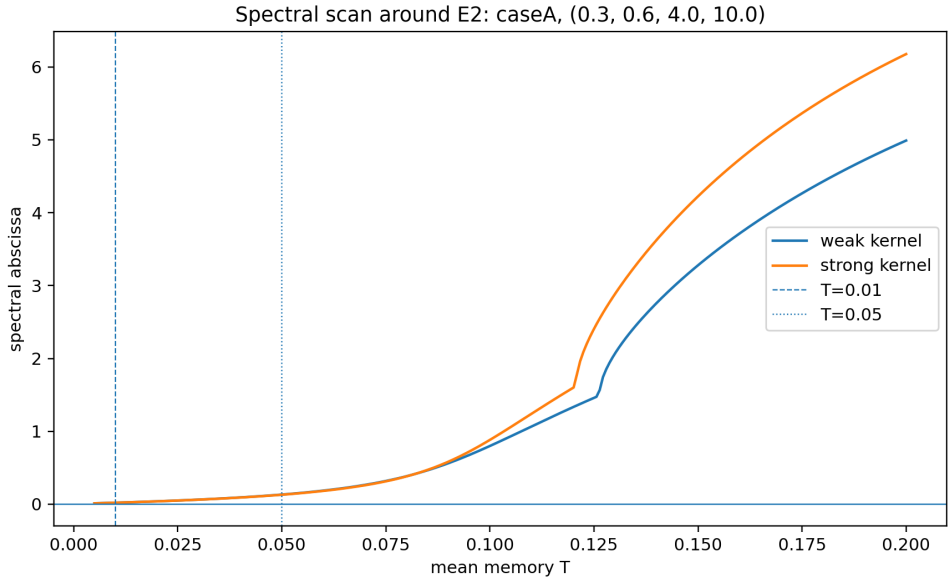

Figure 1. Case A: spectral abscissa versus mean memory T for weak and strong Gamma kernels. The horizontal line is zero; the vertical reference lines mark the two time-domain illustrations, $T = 0.01$ and $T = 0.05$.

The short-memory dynamics at $T = 0.01$ are displayed in Figure 2.

For comparison, Figure 3 shows the larger transient excursions obtained when the mean memory is increased to $T = 0.05$.

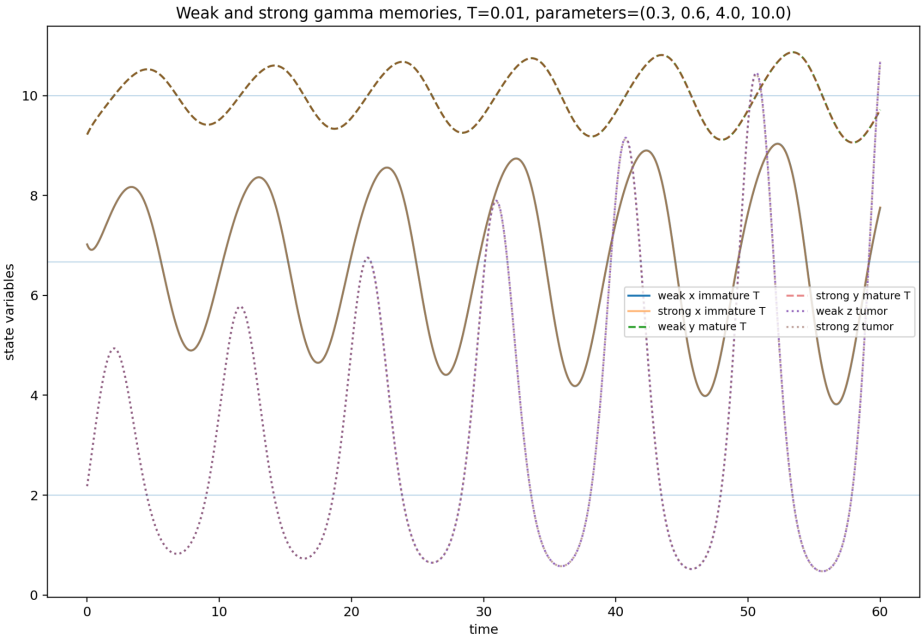

Figure 2. Case A at $T = 0.01$: time traces from the stated perturbation of E_2. The two kernel shapes are close at short mean memory, while the oscillatory departure from coexistence is visible in the tumor and immature-cell components.

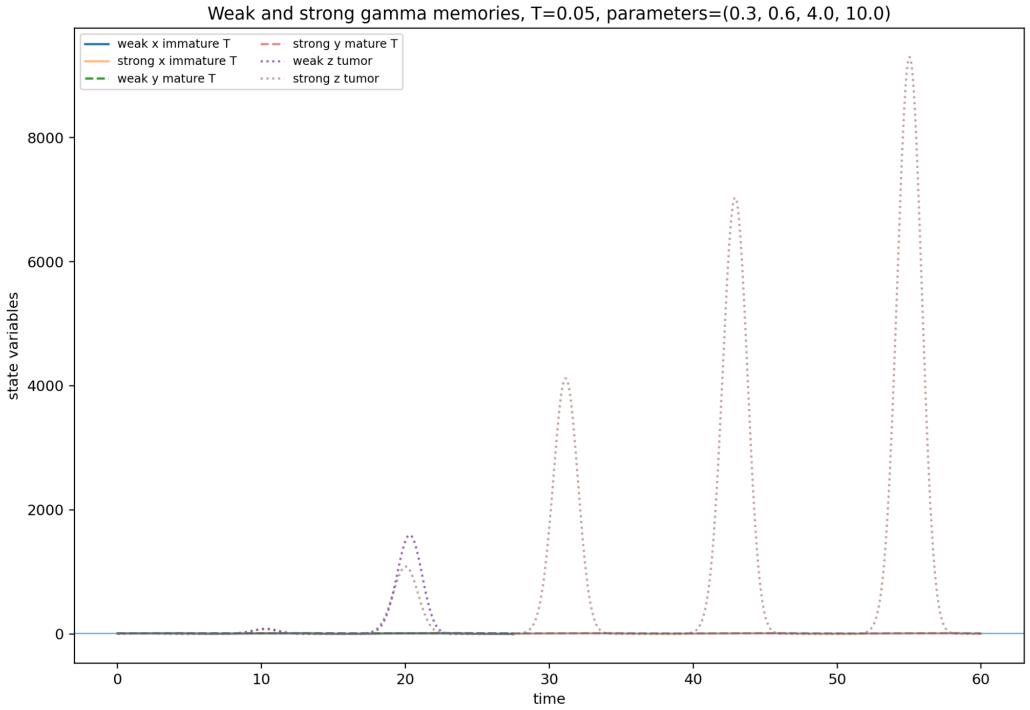

Figure 3. Case A at $T = 0.05$: increasing the mean memory produces larger excursions. The plot is retained as a transient simulation; it does not assert convergence to a bounded attractor.

8.2. Case B: Stability Switch

Case B has $E_2 = (1.75, 7, 0.3333)$. It supplies the cleanest numerical confirmation of the Hopf calculation: as shown in Figure 4, the spectral abscissa is negative at $T = 0.01$ and becomes positive after the refined thresholds in Table 2.

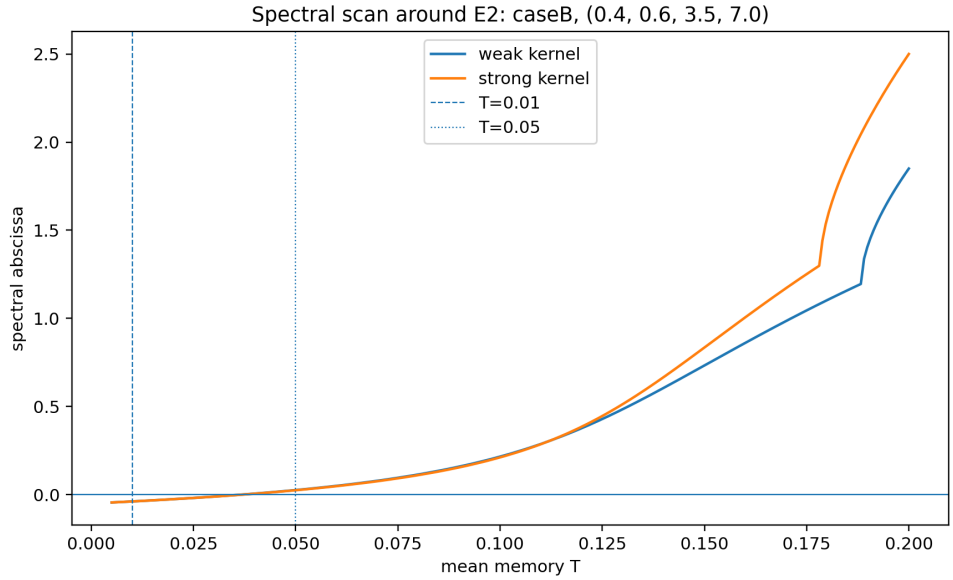

Figure 4. Case B: spectral abscissa versus mean memory. The refined crossings are $T_w^c = 0.036680$ and $T_s^c = 0.036982$; hence, $T = 0.01$ is on the stable side and $T = 0.05$ is on the unstable side for both kernels.

The corresponding stable-side time traces are presented in Figure 5.

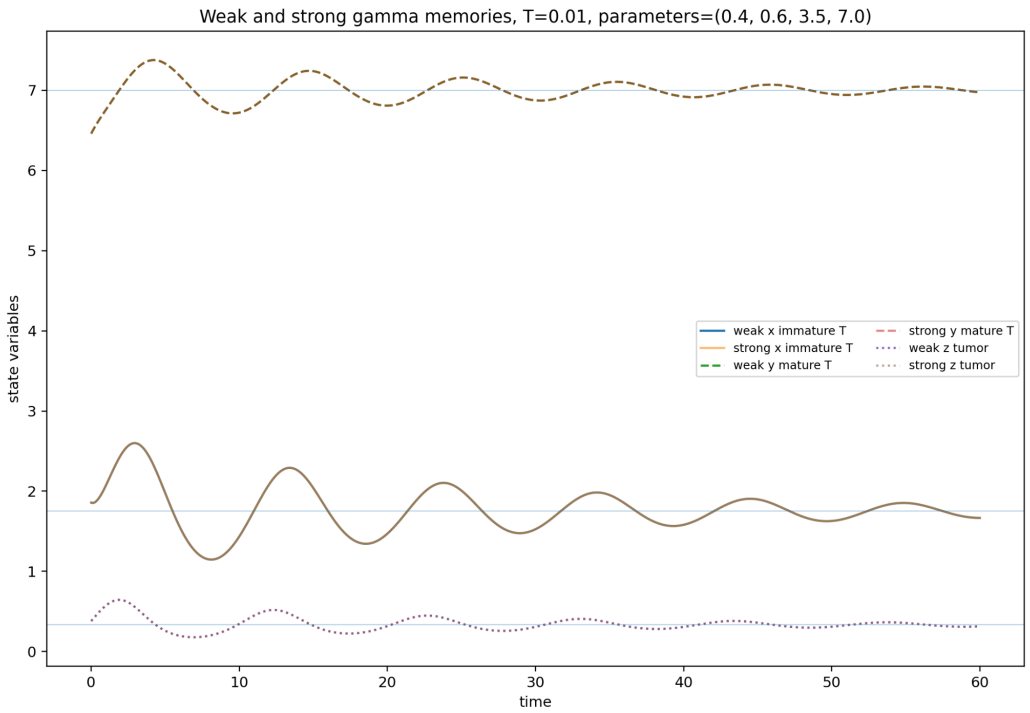

Figure 5. Case B at $T = 0.01$: damped transients approach the coexistence equilibrium, consistent with the negative spectral abscissa.

Beyond the threshold, the loss of contraction toward E_2 is illustrated by the phase portrait in Figure 6.

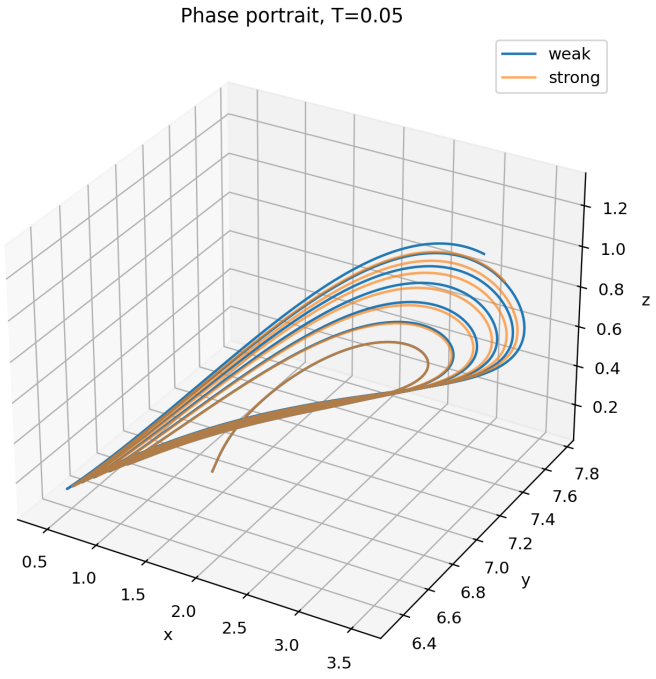

Figure 6. Case B at $T = 0.05$: post-threshold phase portrait. The trajectory no longer contracts to E_2, providing a geometric counterpart to the positive spectral abscissa.

8.3. Cases C and D: Immune Escape and Tumor-Free Stabilization

In case C the formal coexistence equilibrium is not biologically positive. The supplied trajectories display rapid growth beyond the plotting scale, which is consistent with im-

mune escape but unsuitable for a standard linear-scale phase portrait. We therefore report the outcome as an escape regime and do not use the blow-up plots to infer a periodic orbit. In case D the tumor-free state $E_1 = (0, 0.8333, 0)$ is the biologically relevant equilibrium. Figure 7 shows convergence toward that state; the weak and strong solutions are visually almost indistinguishable.

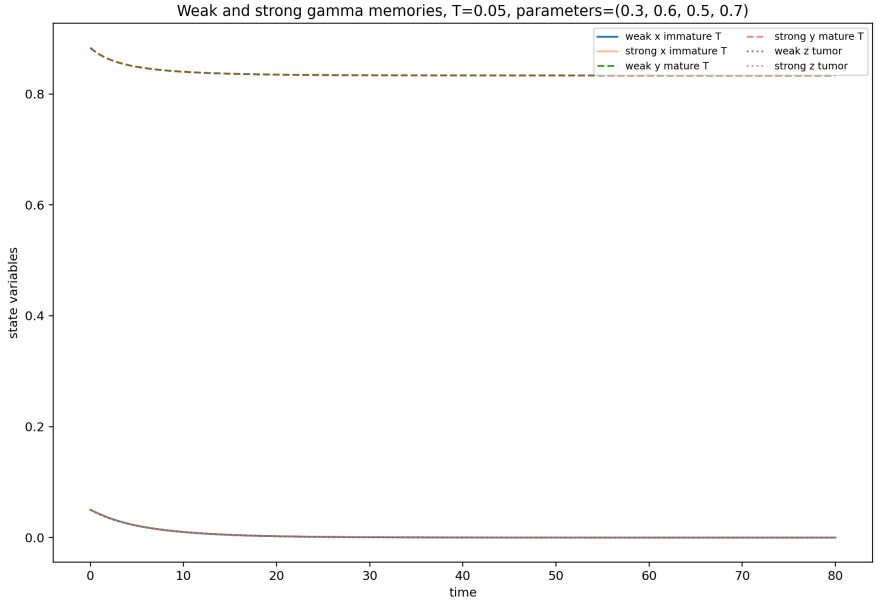

Figure 7. Case D at $T = 0.05$: tumor-free stabilization. The tumor component decreases toward zero while the mature immune component approaches the tumor-free level.

The numerical evidence is therefore used in a deliberately limited way. Figures establish the local-stability narrative in cases A and B and the tumor-free behavior in case D; case C is classified as immune escape because the state leaves the biologically bounded regime. This avoids overinterpreting finite-time plots in regimes with explosive growth.

9. Discussion

The analytical and numerical results show that replacing a fixed delay by a distributed Gamma memory preserves the equilibrium values but changes the stability mechanism. The reason for the first fact is simple: at equilibrium the past history is constant, so every normalized memory kernel returns the same constant value. The reason for the second fact is spectral: the exponential factor of the fixed-delay characteristic equation is replaced by the transfer function of the memory kernel.

The numerical results form a coherent sequence. Case A shows an unstable oscillatory departure from coexistence. Case B is the clearest stability-switch example: the spectral scan predicts stability at $T = 0.01$ and instability at $T = 0.05$, and the time-domain evidence is consistent with this transition. Case C is classified as immune escape because the trajectories leave the biologically bounded regime. Case D shows that, when the tumor-free equilibrium is robustly stable, the memory shape has negligible qualitative effect.

The comparison between weak and strong Gamma kernels is also informative. For short memory lengths, the two kernels often produce nearly overlapping trajectories. Differences become more visible near the stability boundary or in regimes with strong transient amplification. The strong Gamma kernel is more concentrated around its mean and therefore may behave closer to a fixed delay than the weak kernel. This explains why strong memory can produce larger excursions in the oscillatory cases.

Biologically, these observations suggest that not only the average immune-response time but also the distribution of response times may influence tumor–immune dynamics. A broad distribution can smooth the feedback, while a more concentrated distribution can preserve sharper delayed effects and promote oscillations. This distinction is especially relevant near stability thresholds, where small changes in the feedback structure may determine whether coexistence remains stable or turns into recurrent tumor oscillations.

The model also has clear limits. It is spatially homogeneous, deterministic, and normalized; it omits explicit treatment protocols, immune subtypes, tumor heterogeneity, stochasticity and parameter calibration from longitudinal patient data. The Gamma kernels are flexible but still impose a parametric memory shape. These restrictions delimit the present results to mechanism-based comparative dynamics, not clinical prediction. More broadly, the state-transition viewpoint connects with recent energy-landscape approaches in other biomedical dynamical systems, while fractional tumor–immune formulations provide a complementary nonlocal-memory perspective [33,34].

10. Conclusions

This paper introduced weak and strong Gamma distributed memories into a delayed tumor–immune interaction model. The distributed-memory formulation is biologically motivated by the heterogeneity of immune recognition, activation and tumor-cell killing times. By applying the linear chain trick, the weak and strong memory models were written as finite-dimensional ordinary differential systems.

The mathematical analysis proves that the biologically relevant equilibria are preserved, whereas the characteristic equations are modified. Because the delayed feedback enters through coupled products, the characteristic equation contains the second power of the memory transfer function. The weak Gamma kernel therefore leads to a quintic polynomial, while the strong Gamma kernel leads to a seventh-degree polynomial. Routh–Hurwitz criteria and Hopf bifurcation conditions then provide rigorous local stability tests. The simulations, performed with the same benchmark parameter scenarios as the reference delayed model, are consistent with the four qualitative regimes: unstable oscillatory coexistence, stability switching, immune escape and tumor-free stabilization. The most significant differences between weak and strong memories appear near the stability boundary, where the strong Gamma kernel may amplify destabilizing oscillations more clearly. Hence, the distributional form of immune-response memory is a meaningful modeling component, not a secondary technical assumption.

Future work may estimate memory kernels from experimental immune-response data, incorporate treatment thresholds and non-smooth interventions, or combine distributed memory with stochastic perturbations and spatial effects.

Author Contributions: Conceptualization, L.G. and S.R.; Methodology, L.G. and S.R.; Software, L.G. and S.R.; Validation, L.G. and S.R.; Formal analysis, L.G. and S.R.; Investigation, L.G. and S.R.; Resources, L.G. and S.R.; Data curation, L.G. and S.R.; Writing—original draft, L.G. and S.R.; Writing—review & editing, L.G. and S.R.; Visualization, L.G. and S.R.; Supervision, L.G. and S.R.; Project administration, L.G. and S.R. All authors have read and agreed to the published version of the manuscript.

Funding: This research received no external funding.

Data Availability Statement: The original contributions presented in this study are included in the article. Further inquiries can be directed to the corresponding author.

Conflicts of Interest: The authors declare no conflicts of interest.

References

1. Kuznetsov, V.A.; Makalkin, I.A.; Taylor, M.A.; Perelson, A.S. Nonlinear dynamics of immunogenic tumors: Parameter estimation and global bifurcation analysis. *Bull. Math. Biol.* **1994**, *56*, 295–321. [CrossRef]
2. de Pillis, L.G.; Radunskaya, A.E. The dynamics of an optimally controlled tumor model: A case study. *Math. Comput. Model.* **2003**, *37*, 1221–1244. [CrossRef]
3. de Pillis, L.G.; Radunskaya, A.E.; Wiseman, C.L. A validated mathematical model of cell-mediated immune response to tumor growth. *Cancer Res.* **2005**, *65*, 7950–7958. [CrossRef] [PubMed]
4. Dong, Y.; Miyazaki, R.; Takeuchi, Y. Mathematical modeling on helper T cells in a tumor immune system. *Discret. Contin. Dyn. Syst. Ser. B* **2014**, *19*, 55–72. [CrossRef]
5. Dong, Y.; Huang, G.; Miyazaki, R.; Takeuchi, Y. Dynamics in a tumor immune system with time delays. *Appl. Math. Comput.* **2015**, *252*, 99–113. [CrossRef]
6. Li, Y.; Li, D. Long time behavior of a tumor-immune system competition model perturbed by environmental noise. *Adv. Differ. Equ.* **2017**, *2017*, 58. [CrossRef]
7. Dritschel, H.; Waters, S.L.; Roller, A.; Byrne, H.M. A mathematical model of cytotoxic and helper T cell interactions in a tumour microenvironment. *Lett. Biomath.* **2018**, *5*, S36–S68. [CrossRef]
8. Pang, L.; Liu, S.; Zhang, X.; Tian, T. Mathematical modelling and dynamic analysis of anti-tumor immune response. *J. Appl. Math. Comput.* **2020**, *62*, 473–488.
9. Banerjee, S.; Sarkar, R.R. Delay-induced model for tumor-immune interaction and control of malignant tumor growth. *Biosystems* **2008**, *91*, 268–288. [CrossRef] [PubMed]
10. Rihan, F.A.; Safan, M.; Abdeen, M.A.; Rahman, D.A. Qualitative and computational analysis of a mathematical model for tumor-immune interactions. *J. Appl. Math.* **2012**, *2012*, 475720. [CrossRef]
11. Bi, P.; Xiao, H. Bifurcations of tumor-immune competition systems with delay. *Abstr. Appl. Anal.* **2014**, *2014*, 723159. [CrossRef]
12. Khajanchi, S. Chaotic dynamics of a delayed tumor-immune interaction model. *Int. J. Biomath.* **2020**, *13*, 2050009. [CrossRef]
13. Khajanchi, S.; Perc, M.; Ghosh, D. The influence of time delay in a chaotic cancer model. *Chaos* **2018**, *28*, 103101. [CrossRef] [PubMed]
14. Ghosh, D.; Khajanchi, S.; Mangiarotti, S.; Denis, F.; Dana, S.K.; Letellier, C. How tumor growth can be influenced by delayed interactions between cancer cells and the microenvironment? *Biosystems* **2017**, *158*, 17–30. [CrossRef] [PubMed]
15. Yu, M.; Dong, Y.; Takeuchi, Y. Dual role of delay effects in a tumour-immune system. *J. Biol. Dyn.* **2017**, *11*, 334–347. [PubMed]
16. Das, P.; Das, P.; Das, S. Effects of delayed immune-activation in the dynamics of tumor-immune interactions. *Math. Model. Nat. Phenom.* **2020**, *15*, 45. [CrossRef]
17. Kayan, S.; Merdan, H.; Yafia, R.; Goktepe, S. Bifurcation analysis of a modified tumor-immune system interaction model involving time delay. *Math. Model. Nat. Phenom.* **2017**, *12*, 120–145. [CrossRef]
18. Al-Shamrani, N.; Al-Abd, A.M.; Elaiw, A.M. Dynamics of tumor–immune interaction incorporating dendritic cell therapy and two delays. *Math. Biosci. Eng.* **2025**, *22*, 1145–1172.
19. Feng, L.; Yang, Y.; Wang, X. Stability and bifurcation analysis of fractional-order tumor-macrophages interaction model with multi-delays. *Chaos Solitons Fractals* **2023**, *170*, 113357.
20. Dehingia, K.; Sarmah, H.K.; Hosseini, K. Analysis of a delay-induced mathematical model of cancer. *J. Appl. Math. Comput.* **2022**, *68*, 415–438.
21. Liu, Z.; Guo, S.; Wang, Y. Stability and Hopf bifurcation analysis for an age-structured tumor immune model with time delay. *J. Math. Anal. Appl.* **2023**, *528*, 127508.
22. Sardar, M.; Khajanchi, S. Influence of distributed delays on the dynamics of a generalized immune system cancerous cells interactions model. *Int. J. Biomath.* **2024**, *17*, 2350012.
23. Caravagna, G.; d'Onofrio, A.; Milazzo, P. Distributed delays in a hybrid model of tumor-immune system interplay. *J. Theor. Biol.* **2022**, *544*, 111121.
24. MacDonald, N. *Biological Delay Systems: Linear Stability Theory*; Cambridge University Press: Cambridge, UK, 1989.
25. Hale, J.K.; Verduyn Lunel, S.M. *Introduction to Functional Differential Equations*; Springer: New York, NY, USA, 1993.
26. Kuang, Y. *Delay Differential Equations with Applications in Population Dynamics*; Academic Press: Boston, MA, USA, 1993.
27. Smith, H. *An Introduction to Delay Differential Equations with Applications to the Life Sciences*; Springer: New York, NY, USA, 2011.
28. Zhang, T.; Li, Y.; Zhou, J. Data-driven Takagi–Sugeno fuzzy modeling for intermittent control. *Expert Syst. Appl.* **2026**, *328*, 132687. [CrossRef]
29. Freedman, H.I.; Rao, V.S.H. The trade-off between mutual interference and time lags in predator–prey systems. *Bull. Math. Biol.* **1983**, *45*, 991–1004. [CrossRef]
30. Faria, T. Stability and bifurcation for a delayed predator–prey model and the effect of diffusion. *J. Math. Anal. Appl.* **2001**, *254*, 433–463. [CrossRef]
31. Hassard, B.D.; Kazarinoff, N.D.; Wan, Y.H. *Theory and Applications of Hopf Bifurcation*; Cambridge University Press: Cambridge, UK, 1981.

32. Dehingia, K.; Sarmah, H.K.; Alharbi, Y.; Hosseini, K. Mathematical analysis of a cancer model with time-delay in tumor-immune interaction and stimulation processes. *Adv. Differ. Equ.* **2021**, *2021*, 473. [CrossRef] [PubMed]
33. Hassani, H.; Avazzadeh, Z.; Agarwal, P.; Mehrabi, S.; Ebadi, M.J.; Dahaghin, M.S.; Naraghirad, E. A study on fractional tumor–immune interaction model related to lung cancer via generalized Laguerre polynomials. *BMC Med. Res. Methodol.* **2023**, *23*, 189. [CrossRef] [PubMed]
34. Tran, T.M.; Razavi, S.M.; Wu, D.H.; Khanmohammadi, S. Continuous energy landscape model for analyzing brain state transitions. *arXiv* **2026**, arXiv:2601.06991.